Nocturnal Trapping of Agricultural Emissions Drives Persistent Methane Enhancements at the Southern Great Plains

Qingyu Wang[1,6], Xiao-Ming Hu[1,2], Petra Klein[1], Chenghao Wang[1,3], Wesley Honeycutt[4], Ming Xue[1,2], Yu Ding[1], Binbin Weng[3], Adriana E. Larrea Valdivia[5], Yi Yin[6]

[1]School of Meteorology, University of Oklahoma, Norman, OK, USA

[2]Center for Analysis and Prediction of Storms, University of Oklahoma, Norman, OK, USA

[3]Department of Geography and Environmental Sustainability, University of Oklahoma, Norman, OK, USA

[4]School of Electrical & Computer Engineering, University of OK, Norman, Oklahoma, USA

[5]Universidad Nacional de San Agustín de Arequipa, Arequipa, Perú

[6]Department of Environmental Studies, New York University, New York, NY, USA

Corresponding author: Yi Yin (yi.yin@nyu.edu), Xiao-Ming Hu (xhu@ou.edu)

Key Points:

1. An underestimated feeding lot 5.8 km from the SGP tower emits 59-79 kg hr^{-1} of CH_4, over ten times the value from the EDGAR inventory.
2. Strongly stable boundary layers (Ri > 0.4) occur on 26% of nights and trap local CH_4, producing enhancements >300 ppb in the lowest 25 m.
3. Unresolved local sources can dominate CH_4 observations at monitoring sites used for emission inversions and inventory validation.

Abstract

Long-term atmospheric monitoring sites provide the observations used to evaluate greenhouse-gas inventories and constrain atmospheric inversions. The Southern Great Plains (SGP) observatory, among the most heavily utilized sites in the U.S. Department of Energy Atmospheric Radiation Measurement program, has exhibited persistently elevated methane (CH_4) that existing bottom-up inventories cannot explain. Combining multi-year tower observations (2011–2024) with a mobile campaign (June 2024), we trace these CH_4 enhancements to a large animal feeding operation 5.8 km from the site. Mass-balance estimates yield emission rates of 59–79 kg hr^{-1}, exceeding the EDGAR v8.0 agricultural CH_4 for the surrounding 0.1° grid cell (~4 kg hr^{-1}) by more than an order of magnitude. Strongly stable nocturnal boundary layers recurrently trap these emissions near the surface, producing CH_4 enhancements exceeding 300 ppb within the lowest 25 m. These findings demonstrate that underestimated point sources, amplified by boundary-layer trapping, can dominate signals at sites relied upon for inventory validation. Regional inversions that assimilate such local records without resolving the underlying source may systematically overestimate the emissions in the surrounding area.

Plain Language Summary

Scientists rely on long-term monitoring stations to track greenhouse gases and check whether emission reports are accurate. The Southern Great Plains (SGP) site in Oklahoma, one of the most important such stations in the United States, has consistently recorded unusually high methane levels for years, but the reason was unclear. We combined years of station data with a driving survey conducted in June 2024 to search for the source. The data pointed to a large cattle feedlot about 6 km from the station. We estimate this single facility releases about 59–79 kg of methane per hour, more than ten times the amount reported for the entire surrounding area in the widely-used global emission inventory. Calm, stable nighttime weather conditions that are common in this region trap these emissions close to the ground, making the methane buildup especially pronounced. These findings suggest that emission inventories may be missing important individual sources, raising the possibility that other monitoring sites may be similarly affected by unresolved nearby sources.

1 Introduction

Long-term atmospheric monitoring sites provide the continuous, high-precision greenhouse-gas observations that needed for emission inversions, inventory validation, and earth system model evaluation. Tower-based methane (CH_4) records, for example, have been used to infer national emission trends and to constrain regional flux estimates through atmospheric inversions (Jeong et al., 2013; Miller et al., 2013). These applications assume that tower observations are representative of regional-scale signals. When nearby point sources or local meteorological conditions cause the observed concentrations to deviate from this assumption, systematic biases may propagate into the downstream products, from gridded flux estimates to national inventories.

The Southern Great Plains (SGP) observatory is a case in point. As one of the most instrumented greenhouse-gas monitoring sites in the world, SGP provides CH_4 records that serve both as constraints for regional inversions and as reference observations for evaluating bottom-up inventories across south-central United States (Lu et al., 2022; Maasakkers et al., 2023; Miller et al., 2013; Turner et al., 2015). Miller et al. (2013) used SGP records in a geostatistical inversion to show that regional CH_4 emissions in the south-central U.S. are ~2.7 times larger than those in U.S. Environmental Protection Agency (EPA) and Emissions Database for Global Atmospheric Research (EDGAR) inventory values. Similar discrepancies have emerged from tower-based inversions at other locations (Barkley et al., 2023; Cui et al., 2019). The standard interpretation is that bottom-up inventories are biased low. An alternative explanation is also plausible: if an unresolved local source contaminates the tower record, inversions operating at coarser resolution would misattribute its signal to the broader region, inflating the top-down estimate. Meanwhile, many emission quantification frameworks employ Gaussian plume formulations (Albertson et al., 2016; Atherton et al., 2017; Brantley et al., 2014; Caulton et al., 2018) that were developed for

daytime, well-mixed conditions and do not adequately represent dispersion under the strongly stable regimes common at night. The complex boundary layer processes in the U.S. Great Plains (Klein et al., 2016; Klein et al., 2014) alter CH_4 plumes in ways these simplified formulations cannot capture, further preventing inversions from correctly attributing observed enhancements to local emitters.

At SGP, the amplification is especially large: Hu et al. (2025) showed that a fixed-rate CH_4 source produced near-surface enhancements ~40 times larger under early-morning stable conditions than under midday convective mixing at the same distance. Even when nocturnal data are excluded from inversions, morning boundary-layer ventilation and the proximity of the source within the daytime footprint may sustain a residual bias. Here we combine multi-year tower observations (2011–2024), boundary-layer stability analysis, and a targeted mobile campaign (Hu & Wang, 2025) to identify the origin of the persistent CH_4 enhancements at SGP, demonstrating that an unresolved local source, amplified by recurring boundary-layer trapping, can dominate the tower record at a major monitoring site.

2 Data and Methods

2.1 Tower-based CH_4 observations

Continuous CH_4 measurements were collected at the U.S. Department of Energy Atmospheric Radiation Measurement (ARM) Southern Great Plains Central Facility (C1; 36.605°N, 97.488°W; 314 m elevation) near Lamont, Oklahoma (Sisterson et al., 2016). Ambient air was sampled at four intake heights (2, 4, 25, and 60 m above ground level, AGL) using cavity ring-down spectrometers (Picarro G1301/G2301). The analyzer cycled through all four levels within each 20-minute interval, spending 5 minutes at each height, with the final 1 minute of each window was retained as the

reported value (Biraud & Reichl, 2024). The full SGP record (2011–2024) was used for the analysis of diurnal cycles, stability regimes, and wind-direction dependence.

For cross-site comparison, we analyzed hourly CH_4 from three additional U.S. tall-tower sites over 2017–2020, the period with concurrent data availability at all four sites: Park Falls, Wisconsin (LEF), Beech Island, South Carolina (SCT), and Indianapolis, Indiana (INFLUX), obtained from NOAA/GML ObsPack products (Schuldt (2023); Table 1, Fig. S1a). Site coordinates, intake heights, and references are listed in Table 1. At all sites, year-specific annual means were removed from hourly observations to isolate short-term variability, and CH_4 anomalies were defined as deviations from the monthly mean at each measurement height.

Table 1. Tall tower sites used for comparison in this study.

Site Code	Location	Latitude, Longitude	Elevation (masl)	Measurement Height (magl)	Potential main CH_4 emission	Reference
SGP	Lamont, OK	36.6070, - 97.489	314	2,4,**25***,60	Oil and natural gas system, agriculture	Sisterson et al. (2016)
LEF	Park Falls, WI	45.9451, -90.2732	472.0	**30***,122,396	Wetlands	Andrews et al. (2014)
SCT	Beech Island, SC	33.4057, -81.8334	115.2	**31***,61,306	Wetlands	Andrews et al. (2014)
INFLUX (Site 1)	Indianapolis, IN	39.5805, -86.4207	182	**10***, 40,121	Landfills	Davis et al. (2017)

*CH_4 concentrations at these heights are used to compare across the sites.

2.2 Meteorological observations

Surface meteorological variables, including wind speed and direction at 10 m AGL, were obtained from the ARM meteorological station at the SGP C1 facility at 1-minute resolution (Kyrouac &

Tuftedal, 2024). Vertical profiles of temperature, dewpoint, humidity, pressure, and wind were measured by radiosondes launched approximately every 6 hours (00, 06, 12, and 18 UTC) from the SGP launch facility (Atmospheric Radiation Measurement (ARM) user facility, 2001a). These profiles extend from the surface to ~20 km altitude at a high temporal resolution of 2 seconds. Horizontal and vertical wind profiles at 30 m vertical resolution and 15-minute temporal resolution were obtained from a Halo Photonics Streamline Doppler lidar deployed at the C1 facility (Atmospheric Radiation Measurement (ARM) user facility, 2010a, 2010b).

Atmospheric stability was quantified using the gradient Richardson number computed from radiosonde profiles: $R_i = \frac{\frac{g}{\theta_v}\frac{\partial \theta_v}{\partial z}}{\left(\frac{\partial u}{\partial z}\right)^2 + \left(\frac{\partial v}{\partial z}\right)^2}$, where θ_v is the virtual potential temperature, z is height, g is gravitational acceleration (9.81 $m \cdot s^{-2}$), u, v are the wind components. All quantities are obtained from the vertical gradients within a single radiosonde profile rather than from time-averaged turbulent fluxes. Layers with wind shear squared below 10^{-4} s^{-2} were excluded to avoid artificially large values under calm conditions. Values exceeding 0.25 indicate suppressed turbulent mixing, and values above 0.4 correspond to strongly stable conditions (Galperin et al., 2007). In addition to the radiosonde-based gradient Richardson number, we computed a continuous tower-based bulk Richardson number for the case study (Section 3.2) from the 2–60 m virtual potential temperature difference and the 4–60 m wind shear, using tower temperature (60 m, Atmospheric Radiation Measurement (ARM) user facility (2018)) and sonic anemometer winds (4 and 60 m, Atmospheric Radiation Measurement (ARM) user facility (2021)). Because wind is not measured at 2 m, the 4 m level was used as the lower bound for the shear; the resulting slight mismatch in the base heights of the temperature and wind differences has negligible effect on the diagnosed stability regime.

2.3 Mobile field campaign

2.3.1 Field campaign design

To identify and quantify local CH_4 sources near the SGP site, we conducted a mobile survey campaign from June 23–26, 2024 (Hu & Wang, 2025). A LI-COR LI-7810 trace-gas analyzer was mounted on a vehicle and recorded CH_4 dry mole fractions at 1-second temporal resolution (~1.5 m spatial resolution at our typical driving speed). Transects followed a square route (1.6 km × 1.6 km) surrounding a large animal feeding operation (AFO) located 5.8 km to the northwest (312° bearing; Fig. 1). The route was bounded by four county roads: N3070 Rd (east), E0250 Rd (north), N3060 Rd (west), and E0260 Rd (south). Field campaigns were conducted during early morning hours (04:30–07:00 local time, CDT) when the shallow stable boundary layer maximized near-surface CH_4 accumulation and sensitivity to local sources.

Prior to the mobile survey campaign, the vehicle-mounted LI-COR LI-7810 was co-located with the SGP tower Picarro G2301 analyzer at 2 m AGL. Both instruments sampled ambient air simultaneously over a two-hour window (09:00–11:00 local time, CDT) under well-mixed daytime conditions to minimize the influence of vertical gradients on the comparison. The LI-7810 recorded at 1-second resolution; Picarro data were available as hourly averages. The LI-7810 1-second data were averaged to hourly values for a comparison. The mean bias (LI-7810 minus Picarro) was +0.39 ppb with a standard deviation of 0.53 ppb (Fig. S2), well within the manufacturer-specified precision of the LI-7810 (< 1 ppb at 1 s).

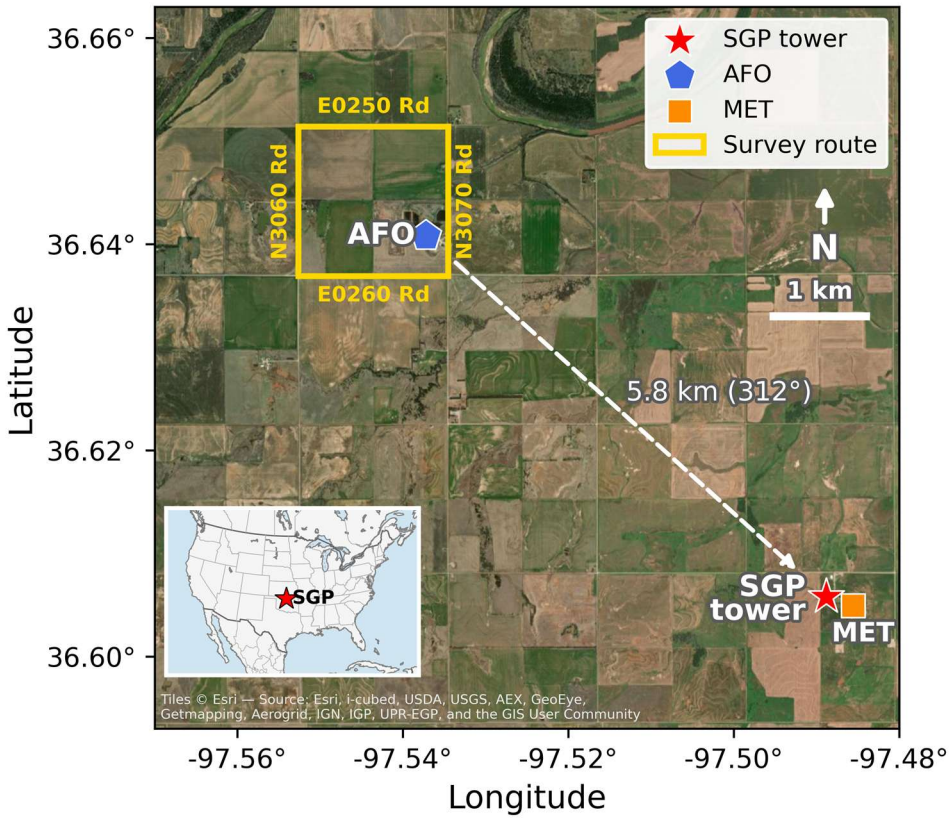


Figure 1. Study area showing the SGP ARM Central Facility CH_4 tower (red star), surface meteorological measurement sation (MET; orange square), and the animal feeding operation (AFO; blue pentagon) 5.8 km to the northwest (312° bearing). The radiosonde launch site is located approximately 200 m north of the tower and is not shown separately at this scale. Yellow lines indicate mobile survey routes during the June 23–26, 2024 campaign. Inset shows the SGP site location within the continental United States.

2.3.2 WRF-GHG simulations

Vertical CH_4 profiles used to extend the surface mobile observations were obtained from WRF-GHG large eddy simulations (LES) configured over the SGP region following Hu et al. (2025). The model uses quadruply nested domains with grid spacings of 12 km, 0.8 km, 160 m, and 32 m. The outermost domain is driven by the operational Global Forecast System (GFS) 0.25° meteorological fields (National Centers for Environmental Prediction, 2015) and Copernicus Atmosphere Monitoring Service (CAMS) global inversion-optimized CH_4 for initial and boundary conditions (Copernicus Atmosphere Monitoring Service, 2020). Anthropogenic CH_4 emissions are

from the Fuel-based Oil and Gas inventory (Francoeur et al., 2021; Gorchov Negron et al., 2018) and wetland emissions from WetCHARTs (Bloom et al., 2017). The outer two domains use the Shin-Hong scale-aware boundary layer scheme (Shin & Hong, 2015), while the inner two domains operate in LES mode with a 1.5-order TKE closure for subgrid-scale mixing. The WRF-GHG framework and its validation are described in Hu et al. (2025), who demonstrated that the 32 m LES successfully reproduces observed CH_4 plume enhancements from a controlled release experiment and from the same AFO examined here. In this study, we used the 32 m domain output at the time step closest to each mobile survey. Only the modeled CH_4 profile shape was retained; the surface concentration was replaced by the in-situ observation at each transect point (Section 2.3.3).

2.3.3 Emission rate estimation

Emission rates from the AFO were estimated using a cross-sectional mass-balance approach (Cambaliza et al., 2014; Lavoie et al., 2015), in which the net CH_4 flux through the four sides of the square survey route was integrated to obtain the total emission rate enclosed within the box. The emission rate is given by:

$$F = M_{\mathrm{CH_4}} \sum_i \sum_k \left(C_{i,k} - C_{i,\mathrm{bg}}\right) \times 10^{-9} \cdot n_k \cdot V_{\perp,i} \cdot \Delta x_i \cdot \Delta z_k$$

where:

F is the CH_4 emission rate (g s^{-1}),

$M_{\mathrm{CH_4}}$ = 16 g mol^{-1} is the molar mass of methane,

Δx_i is the along-transect distance between successive measurement points (m),

$V_{\perp,i}$ is the wind component perpendicular to the transect at point i (m s^{-1}),

190 $C_{i,k}$ is the CH_4 mole fraction at measurement point i and height level k (ppb),

191 $C_{i,\mathrm{bg}}$ is the background CH_4 mole fraction taken from the WRF-GHG profile at the boundary-

192 layer top (ppb),

193 $n_k = P/(RT)$ is the molar air density at level k (mol m^{-3}),

194 Δz_k is the vertical thickness of layer k (m), or the boundary-layer height,

195 10^{-9} converts the mole fraction from ppb to dimensionless mixing ratio.

196 Because the mobile analyzer measures CH_4 only at the surface (~1.5 m AGL), the concentration
197 $C_{i,k}$ at height k required by the mass balance integration was not directly observed. Vertical CH_4
198 profiles were reconstructed at each measurement point i using the profile shape from the
199 concurrent WRF-GHG simulation (32 m horizontal resolution). For each point i, the nearest WRF
200 grid column provided a modeled profile $C_{\mathrm{wrf,k}}$. The capping height k was defined as the lowest
201 WRF level at or above the boundary-layer height diagnosed from the concurrent radiosonde
202 (Section 2.2). The background concentration $C_{i,\mathrm{bg}}$ was taken as $C_{\mathrm{wrf,k}}$.

203 Below the capping height k, the modeled profile was scaled linearly to match the mobile
204 observation $C_{i,obs}$ at the surface while preserving the vertical gradient shape:

205 $$C_{i,k} = C_{i,bg} + \frac{C_{i,obs} - C_{i,bg}}{C_{wrf,k=0} - C_{i,bg}} \cdot (C_{wrf,k} - C_{i,bg})$$

206 Above k, $C_{i,k}$ was set equal to $C_{i,bg}$. This approach retains the WRF-simulated vertical structure
207 while replacing the absolute magnitude.

The perpendicular wind component $V_{\perp}$ was computed geometrically from the wind direction and the outward-pointing normal to each side of the rectangular route, with the sign convention that positive $V_{\perp}$ corresponds to flux directed outward (away from the enclosed AFO). The outward normal direction was determined from the driving direction and the survey orientation (clockwise or counterclockwise), following the right-hand rule.

Uncertainties in the emission estimates were quantified using a Monte Carlo approach (n = 1,000 realizations). In each realization, four key parameters were independently perturbed: wind speed (±1 m s^{-1}, Gaussian), wind direction (±10°, Gaussian), CH_4 concentration (±3% multiplicative, Gaussian), and boundary-layer height (±20% multiplicative, Gaussian). The boundary-layer height perturbation reflects the diagnostic uncertainty inherent in Ri-based methods under stable conditions (Seidel et al., 2010). The emission rate was recalculated for each perturbed realization, and the 5th and 95th percentiles of the resulting distribution define the 90% confidence interval.

We do not perturb the WRF-GHG profile shape or the background concentration in the Monte Carlo ensemble, and direct sensitivity tests show their influence is limited. Since the emission rate is obtained from a closed-path mass balance, a spatially uniform background offset largely cancels around the loop: lowering the boundary-layer top CH_4 by 10 ppb changes the estimate by only less than 1%. The vertical-profile shape is the larger and more state-dependent term. Shifting the boundary-layer height by ±1 model level alters the emission rate by only about −6% to +0.3%, whereas replacing the curved WRF-GHG profile with a fully linear decrease (surface value and boundary-layer height fixed) raises it by ~70%; we regard the latter as a loose upper bound rather than a likely error, since the simulated profiles are consistently curved. We therefore expect these

unaccounted terms to broaden the reported uncertainty range rather than to systematically shift the central estimate.

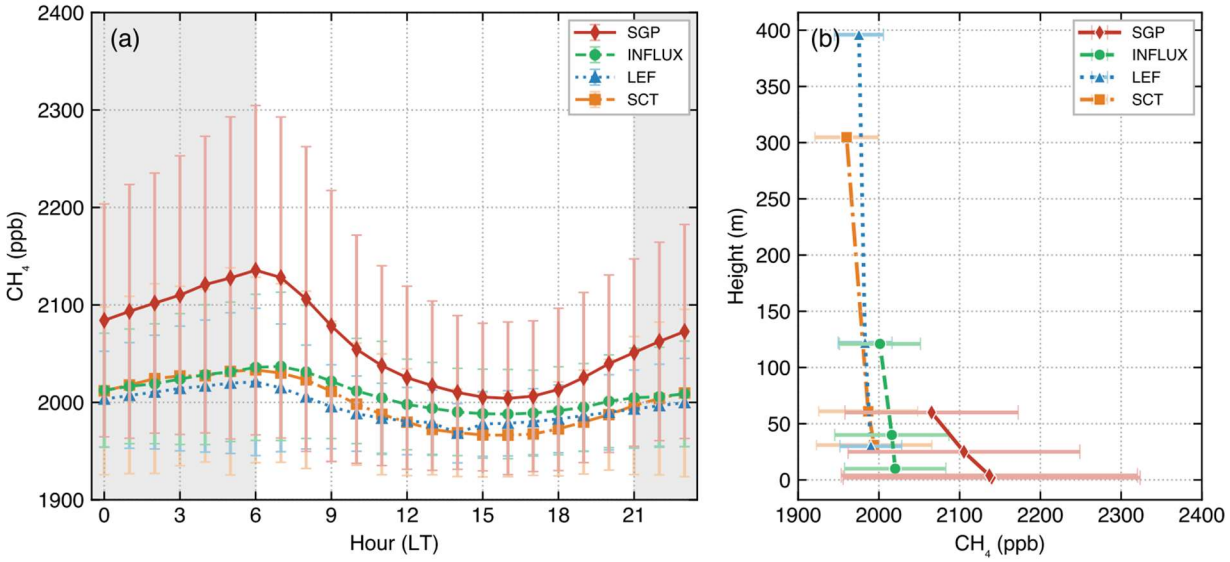


Figure 2. Multi-year (2017–2020) CH_4 comparisons across four U.S. tall tower sites. (a) Mean diurnal cycle of near-surface CH_4 concentration (site information and measurement heights see Table 1). Shaded bands indicate nighttime hours. Error bars denote ±1 standard deviation. (b) Mean nighttime (21:00–06:00 LT) CH_4 vertical profiles. Error bars denote ±1 standard deviation.

3 Results

3.1 The SGP CH_4 enhancements

The SGP site exhibits systematically elevated CH_4 compared with three other U.S. tower sites (LEF, SCT, INFLUX) over 2017–2020 (Fig. 2). Diurnal variations are substantially larger at SGP, with early morning (6AM) near-surface concentrations averaging over 2135 ppb, more than 100 ppb higher than at any other site (Fig. 2a). The vertical structure is also distinctive: average nighttime CH_4 gradients in the lowest 60 m reach 1.27 ppb m^{-1} at SGP, more than triple the gradient at INFLUX (0.37 ppb m^{-1}) and an order of magnitude larger than at LEF or SCT (Fig. 2b). Nocturnal boundary-layer stabilization is common over land, but WRF simulations indicate that SGP develops stronger near-surface stability than the other three sites, with potential

247 temperature inversions below 100 m approximately twice as large despite comparable wind shear
248 profiles (Fig. S3). Strong stratification at SGP is favored by the flat, semi-arid terrain, frequent
249 clear skies, and dry soils, which together maximize net longwave cooling of the surface (Bonin et
250 al., 2015; Klein et al., 2016; Mahrt, 2014). Yet stronger stability alone cannot fully account for the
251 enhancement. A simple plume calculation shows that the EDGAR v8.0 **(**EDGAR Community,
252 2025**)** agricultural CH_4 flux for the grid cell containing SGP (~4 kg hr^{-1}; Fig. S1c) would produce
253 enhancements of only 30–70 ppb at the tower under typical stable conditions (u = 1–2 m s^{-1}, H =
254 100 m), well below the observed nocturnal enhancements routinely exceeding 300 ppb.
255 Reconciling the inventoried emissions with the observed enhancements would require either
256 boundary-layer trapping far stronger than typically observed, or a local source substantially larger
257 than what current inventories attribute to this area, or both.

258 **3.2 Nocturnal boundary-layer trapping: necessary but not sufficient**

259 The night of November 17–18, 2023 illustrates the trapping mechanism in detail. During the
260 afternoon of November 17, convective mixing homogenized CH_4 across all four tower levels near
261 2060 ppb (Fig. 3a). After sunset, radiative cooling established a temperature inversion in the lowest
262 25 m, with $\frac{d\theta}{dz}$ increasing from near zero to 20 K $(100\ m)^{-1}$ by early morning on November 18
263 (Fig. 3b). As the temperature inversion strengthened, the CH_4 profile began to stratify: by 21:00
264 LT the 2 m and 4 m levels had already risen above 2100 ppb while the 60 m level remained near
265 2020 ppb (Fig. 3a). Surface winds remained light (< 2 m s^{-1}) throughout the night, and Ri exceeded
266 0.4 at the time of the nocturnal sonde around 00:00 on November 18, suggesting that turbulent
267 exchange between the surface layer and the atmosphere above had effectively ceased. Under these
268 conditions, any CH_4 emitted into the shallow trapped layer had less mechanism to disperse

vertically.

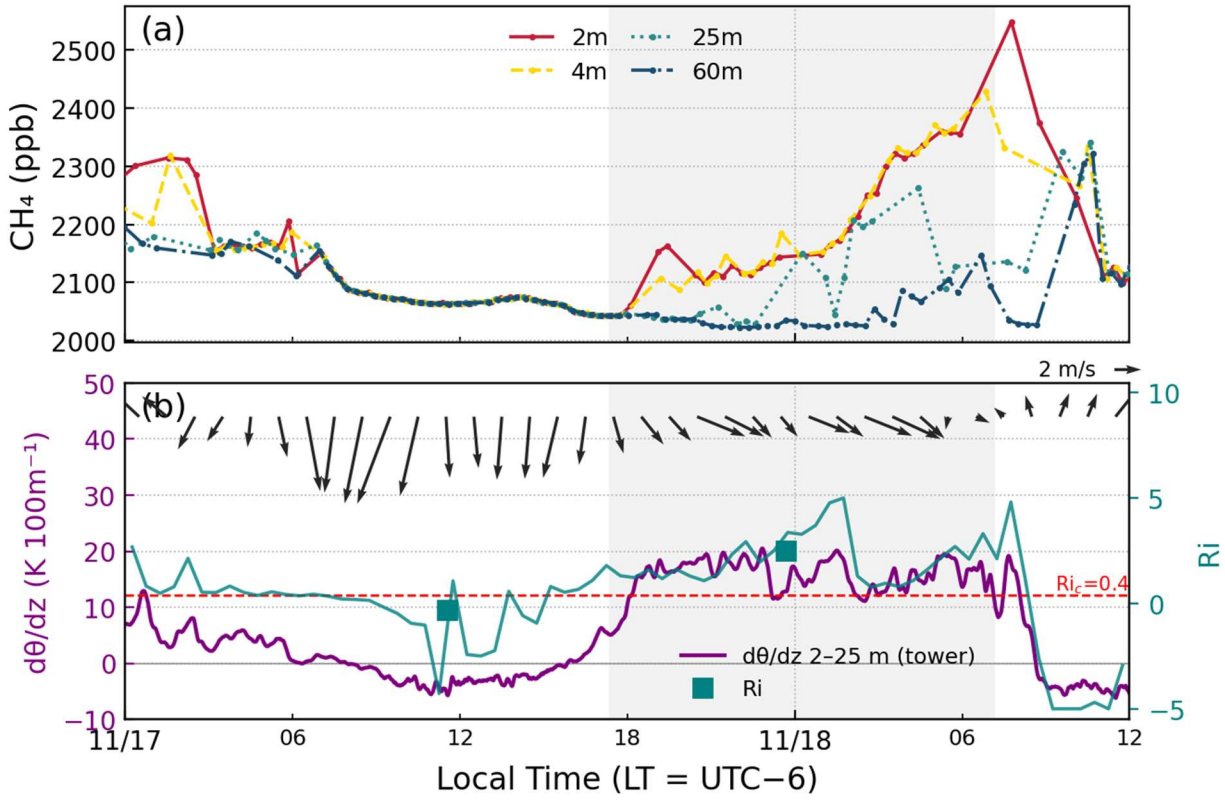
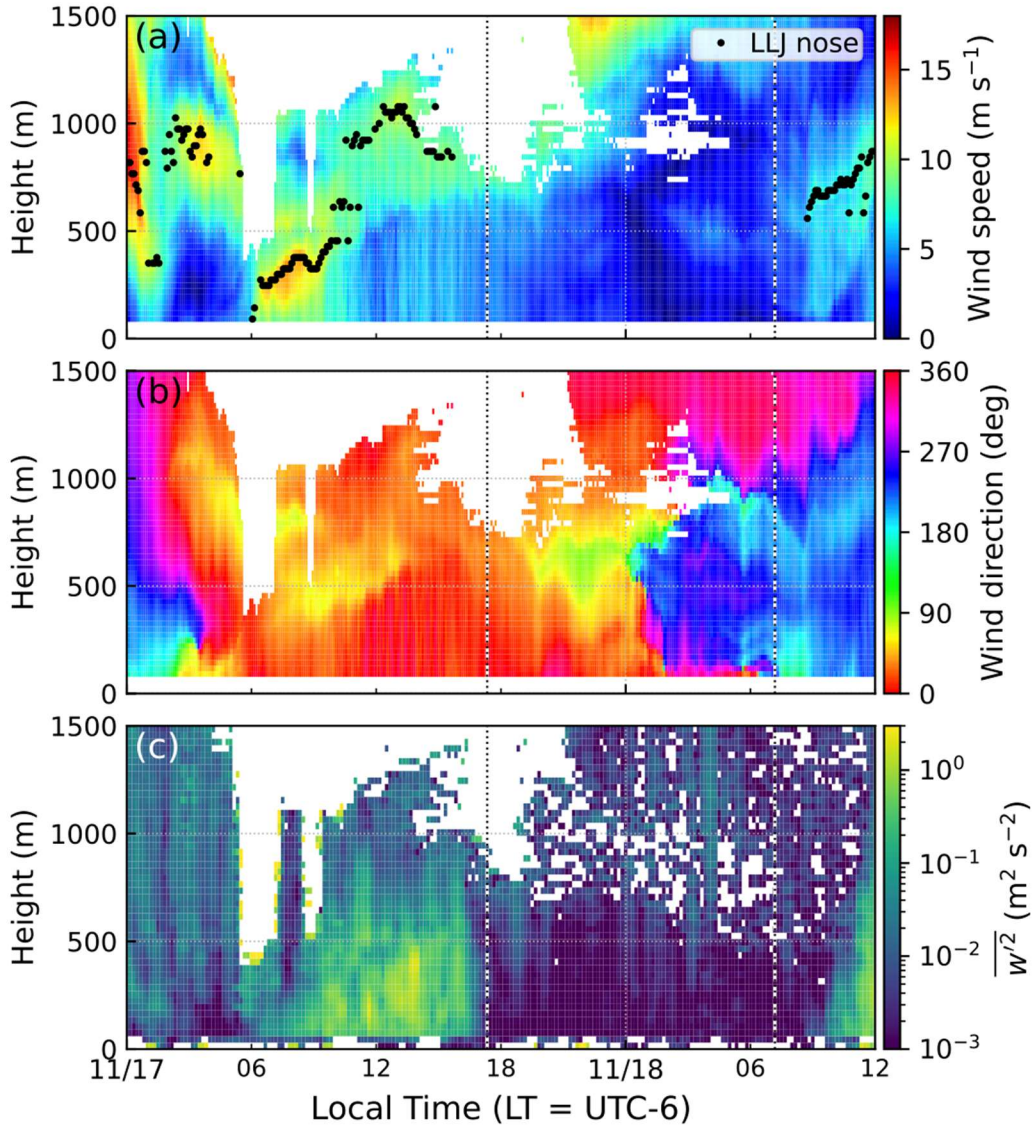


Figure 3. Nighttime CH4 decoupling at SGP, 17–18 Nov 2023 (LT = UTC−6). (a) Tower CH4 at 2, 4, 25 and 60 m; grey shading stands for sunset to sunrise. (b) Near-surface stability: continuous $\frac{d\theta}{dz}$ (2–25 m, left axis) and the bulk Richardson number (right axis) from two sources: a continuous tower estimate (2–60 m temperature gradient with 4–60 m wind shear, teal line) and discrete radiosonde values (lowest ~60 m, teal squares). The dashed line marks Ric = 0.4. Hourly surface wind vectors are shown along the top.

The accumulation proceeded gradually over the following hours. Between 21:00 LT on November 17 and 07:00 LT on November 18, the 2 m concentration rose steadily from ~2120 ppb to a peak of ~2550 ppb, a net increase of approximately 430 ppb (Fig. 3a). CH_4 at 2 m and 4 m remained similar throughout the night, indicating that both heights resided within the same shallow trapped layer. While the 25 m level remained near background until after midnight, when it began a gradual rise to ~2300 ppb by 04:00 LT, suggesting that the trapped layer deepened or that intermittent mixing events partially lofted accumulated CH_4 upward during the second half of the night. The

284 60 m level showed little response, remaining below 2150 ppb until sunrise. At the time of peak
285 stratification near 06:00 LT, the vertical difference between 2 m and 60 m exceeded 450 ppb. The
286 surface winds during this event were from the northwest (~300°; Fig. 3b, Fig. 4b), suggesting
287 potential source from that direction, which will be identified in Section 3.3.

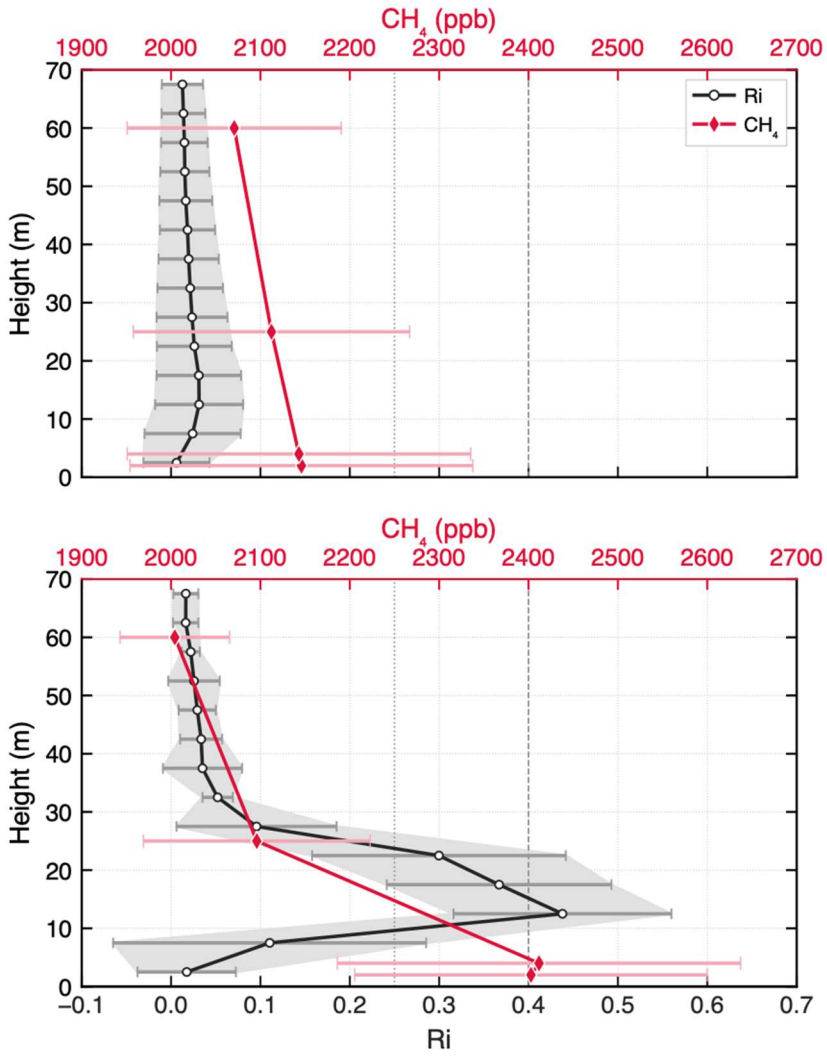


288

289 Figure 4. Doppler-lidar time–height cross-sections at SGP for the night of 17–18 Nov 2023 (LT =
290 UTC−6): (a) horizontal wind speed with the low-level-jet nose (black dots), (b) wind direction,
291 and (c) vertical-velocity variance $\overline{w'^2}$(log scale, turbulence intensity). Dotted lines mark sunset
292 and sunrise. Gates below the instrument Signal-to-Noise Ratio (SNR) threshold are blanked.

The trapping persisted until after sunrise on November 18. As solar heating eroded the surface inversion, $\frac{d\theta}{dz}$ declined from its early-morning peak back toward zero (Fig. 3b), and convective mixing progressively entrained the accumulated CH_4 into a deepening boundary layer. By mid-morning around 09:00, CH_4 at all four levels converged near 2100 ppb (Fig. 3a), effectively diluting the overnight accumulation through a much deeper column. The Doppler lidar (Fig. 4) confirms this transition: the calm, stratified surface layer that persisted throughout the night (Fig. 4ab) gave way to increased vertical velocity variance (Fig. 4c) and a deepening mixed layer after sunrise. The entire cycle, from afternoon homogeneity through nocturnal stratification to morning re-mixing, completed within approximately 18 hours.

Such surface-layer nocturnal CH_4 trapping is common over the Great Plains: over 2011–2024, strongly stable conditions (Ri > 0.4 below 60 m) occurred on 1,227 of 4,693 nights (26%). The SGP site lies in a region characterized by very stable boundary layers, driven by strong radiative cooling over flat terrain and frequent clear skies (Bonin et al., 2015; Klein et al., 2016). On these nights, turbulence shuts down and the surface layer decouples from the atmosphere above. CH_4 accumulates in the resulting trapped layer: near-surface concentrations at 2 m average over 300 ppb higher than at 25 m (Fig. 5b). When Ri remains below 0.25, the 2–25 m CH_4 difference averages only 33 ppb (Fig. 5a), an order of magnitude smaller. Individual stability metrics (wind shear, inversion strength, boundary-layer depth) are each independently consistent with this pattern (Fig. S4): CH_4 anomalies increase with weaker wind shear (Fig. S4a) and stronger potential temperature gradients (Fig. S4b), and the largest anomalies occur under shallow boundary layers accompanied by weak low-level jets (Fig. S4c), consistent with reduced vertical mixing under strongly stable conditions.



315

316 Figure 5. Mean nocturnal profiles of the gradient Richardson number (Ri, black) and CH_4
317 concentration (red) at the SGP site for two stability regimes: (a) weakly stable nights (Ri < 0.25
318 below 45 m) and (b) strongly stable nights (Ri > 0.4 below 45 m). Vertical dashed lines in (b) mark
319 Ri = 0.25 (dotted) and Ri = 0.4 (dashed). Error bars and shading denote ±1 standard deviation.

320 Yet stability alone is insufficient. Many strongly stable nights ($\frac{d\theta}{dz} > 0.1$ K m^{-1}) show negative CH_4
321 anomalies (Fig S4b): the boundary layer trapped clean air, not polluted air. Accumulation requires
322 decoupling and an active upwind source, pointing to emitters absent from current inventories.

323 **3.3 Source identification and emission quantification**

To isolate source signals from meteorological effects, we selected nights with $Ri < 0.25$, when turbulent mixing was active and trapping minimal. Under comparable stability, directional differences in CH_4 enhancement reflect differences in upwind source strength. We binned positive CH_4 anomalies by wind direction over 2011–2024 and computed the 90th-percentile enhancement for each sector (Fig. 6). Two signals stand out. Near 300°, P90 enhancements exceed 250 ppb despite this sector carrying among the fewest observations, pointing to a strong, localized source. A broader enhancement from 140°–240° suggests additional, more diffuse sources to the south.

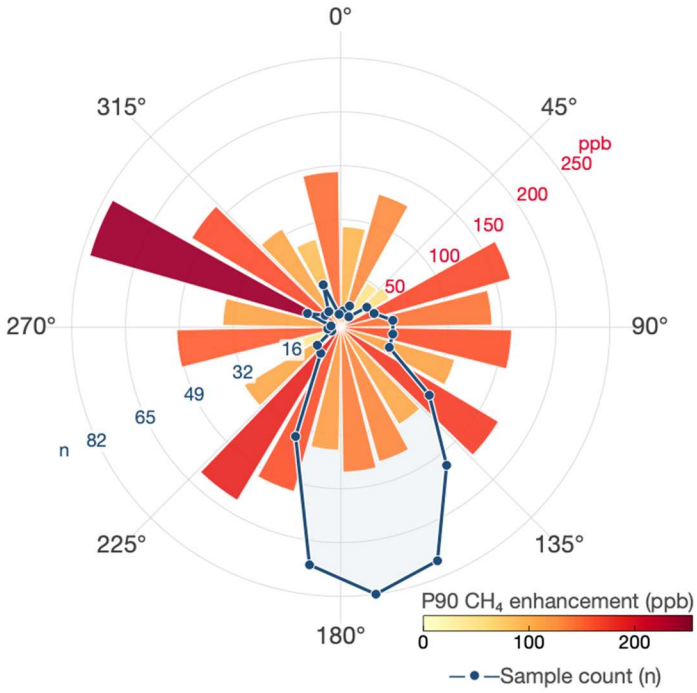


Figure 6.Wind-direction dependence of nocturnal CH_4 enhancements at the SGP tower over 2011–2024, restricted to weakly stable conditions (Ri < 0.25) to minimize confounding by differential trapping. Colored bars show the 90th-percentile CH_4 enhancement for each 15° wind sector; bar length and color both scale with enhancement magnitude. The blue line shows the sample count per sector.

We investigated the 300° sector first. Satellite imagery and ground inspection revealed a large AFO 5.8 km northwest of the tower (Fig. 1). A mobile campaign on four mornings from June 23–26, 2024 (04:30–07:00 LT; Hu and Wang (2025)) consistently recorded elevated CH_4 downwind

of the facility under stable, light-wind conditions. Concentrations peaked on June 26, following a rain event: 6000 ppb near the wastewater pond, above 3000 ppb across the open lots and composting area, against an upwind background of ~2000 ppb. The mass balance method (Section 2.3) yields 59 kg hr^{-1} (90% CI: 43.5, 72.2 kg hr^{-1}) on dry mornings (June 23-25) and 79 kg hr^{-1} on June 26 (90% CI: 51.8–173.4 kg hr^{-1}), with the higher rate likely reflecting enhanced emissions from wet manure. These estimates represent summer conditions. Both enteric and manure CH_4 emissions from feedlot cattle vary with season through changes in ambient temperature, dry matter intake, and herd size, the last of which fluctuates as cattle are periodically sold and restocked. The EDGAR v8.0 inventory assigns ~4 kg hr^{-1} of agricultural CH_4 to the 0.1° grid cell (~100 km^2) containing the AFO (Fig. S1c). The EPA Gridded GHGI (Maasakkers et al., 2023) yields a comparable livestock total of 4.9 kg hr^{-1} for the same area (4.5 kg hr^{-1} enteric fermentation, 0.4 kg hr^{-1} manure management), and a grid-cell total of 12.1 kg hr^{-1} across all sectors including petroleum systems (3.1 kg hr^{-1}) and natural gas production (1.7 kg hr^{-1}). Our measured AFO emissions alone (59–79 kg hr^{-1}) exceed the EDGAR agricultural total for this grid cell by more than an order of magnitude and the EPA grid-cell total across all sectors by a factor of 5–7. This discrepancy likely reflects spatial misallocation rather than a missing source at the county level: EDGAR distributes county-level livestock emissions uniformly across grid cells, so a large concentrated facility is diluted into the surrounding area rather than resolved at its actual location.

The 140°–240° sector was not surveyed but its P90 enhancements (~100–150 ppb; Fig. 6) are roughly half the 300° peak, consistent with diffuse open-range cattle south of the tower. The AFO dominates the SGP enhancement; the southern sources may contribute during frequent southerly flow but remain unquantified. Both source categories are absent from current gridded inventories and are repeatedly amplified by nocturnal stability.

4 Discussion

Our measured AFO emissions (59–79 kg hr^{-1}) exceed the EDGAR v8.0 agricultural CH_4 assigned to the surrounding 0.1° grid cell (~4 kg hr^{-1}) by more than an order of magnitude and the EPA Gridded GHGI total across all sectors (12.1 kg hr^{-1}) by a factor of 5-7. This discrepancy reflects a missing source or a spatial misallocation at the county level: both EDGAR and the EPA Gridded GHGI distribute county-level livestock totals across grid cells using spatial proxies rather than facility-level data (Maasakkers et al., 2023), so a large concentrated facility is diluted into the surrounding area rather than resolved at its actual location. The distinction matters for any application that depends on source-receptor distance. A distributed 4 kg hr^{-1} source at 6 km produces enhancements of only 28–56 ppb at the tower under typical stable conditions (Text S1), whereas the same county-level total concentrated at a single facility 5.8 km away produces the observed enhancements exceeding 300 ppb. Current gridded inventories capture the approximate regional emission budget but cannot reproduce the spatial concentration of emissions that determines the signal at a nearby tower.

Our estimates represent summer conditions, and some temporal variability is expected. Both enteric and manure CH_4 emissions from feedlot cattle vary with season through changes in ambient temperature and dry matter intake, and herd size fluctuates as cattle are periodically sold and restocked. However, even the lower bound of our estimates (59 kg hr^{-1}) exceeds the grid-cell inventory total by a wide margin, and the core finding that emissions are spatially concentrated at a level unresolved by current inventories is independent of the precise emission rate.

Tower-based CH_4 records from SGP have been used to infer that regional emissions in the south-central U.S. are substantially higher than bottom-up inventories indicate. Our results introduce an alternative mechanism that could contribute to this discrepancy: if a strong local source influences

386 the tower record, inversions operating at coarser resolution would misattribute its signal to the
387 broader region, inflating the top-down estimate. At SGP, the AFO produces enhancements at the
388 tower an order of magnitude larger under stable conditions than under well-mixed conditions (Hu
389 et al., 2025), and strongly stable conditions occur on 26% of nights, so inversions that retain
390 nocturnal data would be particularly susceptible. Our results thus show that the assumption of
391 regional representativeness at SGP is compromised by a local source that current inversions cannot
392 resolve.

393 The local source influence documented here is not unique to SGP. Similar biases can arise
394 wherever three conditions co-occur: a strong point source within the typical nocturnal footprint of
395 the tower, frequent strongly stable stratification that traps emissions in a shallow surface layer, and
396 emission inventories that lack facility-level resolution. Agricultural regions with concentrated
397 animal feeding operations and energy-producing basins with clustered well pads are settings where
398 these conditions may be met, and the rapid expansion of both across the central United States over
399 the past two decades means that monitoring sites established in once-rural settings may
400 increasingly lie within the footprint of sources that were absent or far smaller when the sites were
401 commissioned. The wind-direction-dependent analysis of CH_4 enhancements under well-mixed
402 conditions presented here (Fig. 6) provides a straightforward diagnostic for identifying directional
403 biases at other tower sites without requiring dedicated field campaigns.

404 Once detected, can the local influence be removed so the record still constrains regional emissions?
405 Three strategies offer partial remedies. Wind direction filtering is the most direct, at the cost of
406 discarding regional information carried by northwesterly flow. Restricting the analysis to
407 afternoon, well-mixed conditions reduces the nocturnal bias but does not remove it, since morning
408 ventilation lofts accumulated CH_4 into the daytime boundary layer and the AFO remains within

the daytime footprint. Most completely, the AFO can be added to the inversion prior as a point source with a measured emission rate, allowing the transport model to account for its contribution rather than aliasing it onto the regional flux. These approaches are complementary, and their relative value will depend on the inversion framework. Testing them quantitatively is beyond our present scope but is a natural next step.

5 Conclusions

This study identifies the origin of the persistent CH_4 enhancement at the SGP ARM site: a large animal feeding operation 5.8 km from the tower, with estimated emissions of 59–79 kg hr^{-1} across four survey days. This single facility exceeds the EDGAR v8.0 agricultural inventory for the surrounding 0.1° grid cell by more than an order of magnitude. On 26% of nights over 2011–2024, strongly stable conditions ($Ri > 0.4$) trap these emissions near the surface, producing CH_4 gradients exceeding 300 ppb within the lowest 25 m. These results carry broader implications. Tower-based CH_4 records are widely used to constrain emission inversions and validate gridded inventories, applications that assume the observed enhancement is regionally representative. We show that a single sub-grid source, amplified by recurring boundary-layer trapping, can violate this assumption. Other monitoring sites in agricultural or energy-producing regions with frequent nocturnal stratification may be similarly vulnerable. Wind-direction-dependent analysis of CH_4 anomalies under well-mixed conditions provides a straightforward diagnostic for identifying affected sites. Ensuring that such contamination does not propagate into regional and national emission estimates will require both systematic near-source characterization at key tower sites and inversion frameworks capable of resolving stable boundary-layer dynamics.

Acknowledgments

This work was supported by Department of Energy, National Energy Technology Lab Grant Number DE-FE00322292 and grant no. 20163646499 from the Universidad Nacional de San Agustín de Arequipa (UNSA) of Peru through the IREES/LASI Global Change and Human Health Institute.

Open Research

The mobile measurement data are available at Hu and Wang (2025). Meteorological data used in this study are all from the SGP ARM site, including surface meteorological instrumentation (Atmospheric Radiation Measurement (ARM) user facility, 1993), Ballon-borne sounding system (Atmospheric Radiation Measurement (ARM) user facility, 2001a), Doppler lidar horizontal wind speed and direction (Atmospheric Radiation Measurement (ARM) user facility, 2010a), and Doppler lidar vertical velocity (Atmospheric Radiation Measurement (ARM) user facility, 2010b). Air temperature at 25m and 60m is used for the case study on November 17-18, 2023 is available at Atmospheric Radiation Measurement (ARM) user facility (2018). Wind speed and direction at 4m and 60m for the case study is at Atmospheric Radiation Measurement (ARM) user facility (2021). SGP site CH_4 concentration data are available at Atmospheric Radiation Measurement (ARM) user facility (2001b). LEF, SCT, and INFLUX CH_4 data are from ObsPack (Masarie et al., 2014). EDGAR datasets are available at EDGAR Community (2025), and EPA Greenhouse Gas Inventory (GHGI) are at Maasakkers et al. (2023). WRF-GHG configurations follow Hu et al. (2025). In the WRF-GHG, Copernicus Atmosphere Monitoring Service (CAMS) global inversion-optimized CH_4 (Copernicus Atmosphere Monitoring Service, 2020) is used for initial and boundary conditions.

Conflict of Interest Disclosure

The authors declare no conflicts of interest relevant to this study.

References

Albertson, J. D., Harvey, T., Foderaro, G., Zhu, P., Zhou, X., Ferrari, S., et al. (2016). A mobile sensing approach for regional surveillance of fugitive methane emissions in oil and gas production. *Environmental science & technology, 50*(5), 2487-2497. https://doi.org/10.1021/acs.est.5b05059

Andrews, A., Kofler, J., Trudeau, M., Williams, J., Neff, D., Masarie, K., et al. (2014). CO2, CO, and CH4 measurements from tall towers in the NOAA Earth System Research Laboratory's Global Greenhouse Gas Reference Network: Instrumentation, uncertainty analysis, and recommendations for future high-accuracy greenhouse gas monitoring efforts. *Atmospheric Measurement Techniques, 7*(2), 647-687. https://doi.org/10.5194/amt-7-647-2014

Atherton, E., Risk, D., Fougère, C., Lavoie, M., Marshall, A., Werring, J., et al. (2017). Mobile measurement of methane emissions from natural gas developments in northeastern British Columbia, Canada. *Atmospheric Chemistry and Physics, 17*(20), 12405-12420. https://doi.org/10.5194/acp-17-12405-2017

Atmospheric Radiation Measurement (ARM) user facility. (1993). *Surface Meteorological Instrumentation (MET). 1993-07-21 to 2024-10-06, Southern Great Plains (SGP) Lamont, OK (Extended and Co-located with C1) (E13). [Dataset]. Compiled by J. Kyrouac, Y. Shi and M. Tuftedal. http://dx.doi.org/10.5439/1786358*.

Atmospheric Radiation Measurement (ARM) user facility. (2001a). *Balloon-Borne Sounding System (SONDEWNPN). 2001-04-01 to 2024-10-08, Southern Great Plains (SGP) Central Facility, Lamont, OK (C1) [Dataset]. Compiled by E. Keeler, K. Burk and J. Kyrouac. https://doi.org/10.5439/1595321*.

Atmospheric Radiation Measurement (ARM) user facility. (2001b). *Precision Carbon Dioxide Mixing Ratio System (PGS), 2001-04-11 to 2024-10-08, Southern Great Plains (SGP) Central Facility, Lamont, OK (C1) [Dataset]. Compiled by S. Biraud, A. Moyes and K. Reichl. http://dx.doi.org/10.5439/1342969*.

Atmospheric Radiation Measurement (ARM) user facility. (2010a). *Doppler Lidar Horizontal Wind Profiles (DLPROFWIND4NEWS). 2010-11-02 to 2024-04-25, Southern Great Plains (SGP) Central Facility, Lamont, OK (C1) [Dataset]. Compiled by T. Shippert, R. Newsom, L. Riihimaki and D. Zhang. ARM Data Center. http://dx.doi.org/10.5439/1178582*.

Atmospheric Radiation Measurement (ARM) user facility. (2010b). *Doppler Lidar Wind Statistics Profiles (DLPROFWSTATS4NEWS). 2010-10-22 to 2023-10-23, Southern Great Plains (SGP) Central Facility, Lamont, OK (C1) [Dataset]. Compiled by T. Shippert, R. Newsom, L. Riihimaki and D. Zhang. ARM Data Center. http://dx.doi.org/10.5439/1178583*.

Atmospheric Radiation Measurement (ARM) user facility. (2018). *Facility-specific multi-level Meteorological Instrumentation (TOWERMET), 2018-12-04 to 2026-09-07, Southern Great Plains (SGP) Central Facility, Lamont, OK (C1). [Dataset]. Compiled by J. Kyrouac, Y. Shi and M. Tuftedal. ARM Data Center. Data set accessed 2026-09-08 at http://dx.doi.org/10.5439/1501941*.

Atmospheric Radiation Measurement (ARM) user facility. (2021). *Carbon Dioxide Flux Measurement Systems (CO2FLXWIND), 2021-01-03 to 2026-09-05, Southern Great Plains (SGP) Central Facility, Lamont, OK (C1) [Dataset]. Compiled by A. Koontz, S. Biraud and S. Chan. ARM Data Center. Data set accessed 2026-09-08 at http://dx.doi.org/10.5439/1365398*.

Barkley, Z., Davis, K., Miles, N., Richardson, S., Deng, A., Hmiel, B., et al. (2023). Quantification of oil and gas methane emissions in the Delaware and Marcellus basins using a network of continuous tower-based measurements. *Atmos. Chem. Phys., 23*(11), 6127-6144. https://acp.copernicus.org/articles/23/6127/2023/

Biraud, S., & Reichl, K. (2024). *Precision Gas System (PGS) Instrument Handbook*. Retrieved from http://www.arm.gov/publications/tech_reports/handbooks/pgs_handbook.pdf

Bloom, A. A., Bowman, K. W., Lee, M., Turner, A. J., Schroeder, R., Worden, J. R., et al. (2017). A global wetland methane emissions and uncertainty dataset for atmospheric chemical transport models (WetCHARTs version 1.0). *Geoscientific Model Development, 10*(6), 2141-2156. https://doi.org/10.5194/gmd-10-2141-2017

Bonin, T. A., Blumberg, W. G., Klein, P. M., & Chilson, P. B. (2015). Thermodynamic and Turbulence Characteristics of the Southern Great Plains Nocturnal Boundary Layer Under Differing Turbulent Regimes. *Boundary-Layer Meteorology, 157*(3), 401-420. https://doi.org/10.1007/s10546-015-0072-2

Brantley, H. L., Thoma, E. D., Squier, W. C., Guven, B. B., & Lyon, D. (2014). Assessment of methane emissions from oil and gas production pads using mobile measurements. *Environmental science & technology, 48*(24), 14508-14515. https://doi.org/10.1021/es503070q

Cambaliza, M. O. L., Shepson, P. B., Caulton, D. R., Stirm, B., Samarov, D., Gurney, K. R., et al. (2014). Assessment of uncertainties of an aircraft-based mass balance approach for quantifying urban greenhouse gas emissions. *Atmos. Chem. Phys., 14*(17), 9029-9050. https://acp.copernicus.org/articles/14/9029/2014/

Caulton, D. R., Li, Q., Bou-Zeid, E., Fitts, J. P., Golston, L. M., Pan, D., et al. (2018). Quantifying uncertainties from mobile-laboratory-derived emissions of well pads using inverse Gaussian methods. *Atmospheric Chemistry and Physics, 18*(20), 15145-15168. https://doi.org/10.5194/acp-18-15145-2018

Copernicus Atmosphere Monitoring Service. (2020). *CAMS global inversion-optimised greenhouse gas fluxes and concentrations. [Dataset] Copernicus Atmosphere Monitoring Service (CAMS) Atmosphere Data Store. https://doi.org/10.24381/ed2851d2*.

Cui, Y. Y., Vijayan, A., Falk, M., Hsu, Y.-K., Yin, D., Chen, X. M., et al. (2019). A Multiplatform Inversion Estimation of Statewide and Regional Methane Emissions in California during 2014–2016. *Environmental science & technology, 53*(16), 9636-9645. https://doi.org/10.1021/acs.est.9b01769

Davis, K. J., Deng, A., Lauvaux, T., Miles, N. L., Richardson, S. J., Sarmiento, D. P., et al. (2017). The Indianapolis Flux Experiment (INFLUX): A test-bed for developing urban greenhouse gas emission measurements. *Elem Sci Anth, 5*, 21. https://doi.org/10.1525/elementa.188

EDGAR Community. (2025). *EDGAR (Emissions Database for Global Atmospheric Research) Community GHG Database, a collaboration between the European Commission, Joint Research Centre (JRC), the International Energy Agency (IEA), and comprising IEA-EDGAR CO2, EDGAR CH4, EDGAR N2O, EDGAR F-GASES version*

EDGAR_2025_GHG. European Commission, JRC [Dataset]. https://edgar.jrc.ec.europa.eu/dataset_ghg2025#p4.

Francoeur, C. B., McDonald, B. C., Gilman, J. B., Zarzana, K. J., Dix, B., Brown, S. S., et al. (2021). Quantifying Methane and Ozone Precursor Emissions from Oil and Gas Production Regions across the Contiguous US. *Environmental science & technology, 55*(13), 9129-9139. https://doi.org/10.1021/acs.est.0c07352

Galperin, B., Sukoriansky, S., & Anderson, P. S. (2007). On the critical Richardson number in stably stratified turbulence. *Atmospheric Science Letters, 8*(3), 65-69. https://doi.org/10.1002/asl.153

Gorchov Negron, A. M., McDonald, B. C., McKeen, S. A., Peischl, J., Ahmadov, R., de Gouw, J. A., et al. (2018). Development of a Fuel-Based Oil and Gas Inventory of Nitrogen Oxides Emissions. *Environmental science & technology, 52*(17), 10175-10185. https://doi.org/10.1021/acs.est.8b02245

Hu, X. M., Honeycutt, W. T., Wang, C., Weng, B., Zhou, B., & Xue, M. (2025). Observation and simulation of methane plumes during the morning boundary layer transition. *Journal of Geophysical Research: Atmospheres, 130*(7), e2024JD042317. https://doi.org/10.1029/2024JD042317

Hu, X. M., & Wang, Q. (2025). *Source Attribution of Methane Enhancements at the Southern Great Plains Atmospheric Radiation Measurement Site Field Campaign Report. Methane Analyzer. [Dataset]. ARM Data Center.* https://www.arm.gov/research/campaigns/sgp2024MMC.

Jeong, S., Hsu, Y. K., Andrews, A. E., Bianco, L., Vaca, P., Wilczak, J. M., & Fischer, M. L. (2013). A multitower measurement network estimate of California's methane emissions. *Journal of Geophysical Research: Atmospheres, 118*(19), 11,339-311,351. https://doi.org/10.1002/jgrd.50854

Klein, P. M., Hu, X.-M., Shapiro, A., & Xue, M. (2016). Linkages between boundary-layer structure and the development of nocturnal low-level jets in central Oklahoma. *Boundary-Layer Meteorology, 158*(3), 383-408. https://doi.org/10.1007/s10546-015-0097-6

Klein, P. M., Hu, X.-M., & Xue, M. (2014). Impacts of mixing processes in nocturnal atmospheric boundary layer on urban ozone concentrations. *Boundary-Layer Meteorology, 150*, 107-130. https://doi.org/10.1007/s10546-013-9864-4

Kyrouac, J., & Tuftedal, M. (2024). *Surface Meteorological System (MET) Instrument Handbook*. Retrieved from United States: https://www.osti.gov/biblio/1007926

Lavoie, T. N., Shepson, P. B., Cambaliza, M. O. L., Stirm, B. H., Karion, A., Sweeney, C., et al. (2015). Aircraft-Based Measurements of Point Source Methane Emissions in the Barnett Shale Basin. *Environmental science & technology, 49*(13), 7904-7913. https://doi.org/10.1021/acs.est.5b00410

Lu, X., Jacob, D. J., Wang, H., Maasakkers, J. D., Zhang, Y., Scarpelli, T. R., et al. (2022). Methane emissions in the United States, Canada, and Mexico: evaluation of national methane emission inventories and 2010–2017 sectoral trends by inverse analysis of in situ (GLOBALVIEWplus CH4 ObsPack) and satellite (GOSAT) atmospheric observations. *Atmospheric Chemistry and Physics, 22*(1), 395-418. https://doi.org/10.5194/acp-22-395-2022

Maasakkers, J. D., McDuffie, E. E., Sulprizio, M. P., Chen, C., Schultz, M., Brunelle, L., et al. (2023). *A gridded inventory of annual 2012–2018 US anthropogenic methane emissions. [Dataset]*. https://doi.org/10.5281/zenodo.8367082.

Mahrt, L. (2014). Stably stratified atmospheric boundary layers. *Annual review of fluid mechanics, 46*(1), 23-45. https://doi.org/10.1146/annurev-fluid-010313-141354

Masarie, K., Peters, W., Jacobson, A., & Tans, P. (2014). *ObsPack: a framework for the preparation, delivery, and attribution of atmospheric greenhouse gas measurements. [Dataset] Earth System Science Data.* https://commons.datacite.org/doi.org/10.25925/20251001.

Miller, S. M., Wofsy, S. C., Michalak, A. M., Kort, E. A., Andrews, A. E., Biraud, S. C., et al. (2013). Anthropogenic emissions of methane in the United States. *Proceedings of the National Academy of Sciences, 110*(50), 20018-20022. https://doi.org/10.1073/pnas.1314392110

National Centers for Environmental Prediction, N. W. S. N. U. S. D. o. C. (2015). *NCEP GFS 0.25 Degree Global Forecast Grids Historical Archive*. Retrieved from: https://doi.org/10.5065/D65D8PWK

Schuldt, K. N., Aalto, T., Andrews, A., Aoki, S., Arduini, J., Baier, B., Bergamaschi, P., Biermann, T., Biraud, S. C., Boenisch, H., Brailsford, G., Chen, H., Colomb, A., Conil, S., Cristofanelli, P., Cuevas, E., Daube, B., Davis, K., Mazière, M. D., Delmotte, M., Desai, A., DiGangi, J. P., Dlugokencky, E., Elkins, J. W., Emmenegger, L., Fischer, M. L., Gatti, L. V., Gehrlein, T., Gerbig, C., Gloor, E., Goto, D., Haszpra, L., Hatakka, J., Heimann, M., Heliasz, M., Hermanssen, O., Hintsa, E., Holst, J., Ivakhov, V., Jaffe, D., Joubert, W., Kang, H.-Y., Karion, A., Kazan, V., Keronen, P., Ko, M.-Y., Kominkova, K., Kort, E., Kozlova, E., Krummel, P., Kubistin, D., Labuschagne, C., Langenfelds, R., Laurent, O., Laurila, T., Lauvaux, T., Lee, J., Lee, H., Lee, C.H., Lehner, I., Leppert, R., Leuenberger, M., Lindauer, M., Loh, Z., Lopez, M., Machida, T., Mammarella, I., Manca, G., Marek, M. V., Martin, M. Y., Matsueda, H., McKain, K., Miles, N., Miller, C. E., Miller, J. B., Moore, F., Morimoto, S., Munro, D., Myhre, C. L., Mölder, M., Müller-Williams, J., Nichol, S., Niwa, Y., ODʹoherty, S., Obersteiner, F., Piacentino, S., Pichon, J. M., Pittman, J., Plass-Duelmer, C., Ramonet, M., Richardson, S., Rivas, P. P., Saito, K., Santoni, G., Sasakawa, M., Scheeren, B., Schuck, T., Schumacher, M., Seifert, T., Sha, M. K., Shepson, P., Sloop, C. D., Smith, P., Steinbacher, M., Stephens, B., Sweeney, C., Timas, H., Torn, M., Trisolino, P., Turnbull, J., Tørseth, K., Viner, B., Vitkova, G., Watson, A., Wofsy, S., Worsey, J., Worthy, D., Zahn, A., and di Sarra, A. G. . (2023). *Multi-laboratory compilation of atmospheric methane data for the period 1983-2022; obspack_ch4_1_GLOBALVIEWplus_v6.0_2023-12-01. [Dataset]. NOAA Global Monitoring Laboratory.* https://doi.org/10.25925/20241101.

Seidel, D. J., Ao, C. O., & Li, K. (2010). Estimating climatological planetary boundary layer heights from radiosonde observations: Comparison of methods and uncertainty analysis. *Journal of Geophysical Research: Atmospheres, 115*(D16). https://doi.org/10.1029/2009JD013680

Shin, H. H., & Hong, S.-Y. (2015). Representation of the Subgrid-Scale Turbulent Transport in Convective Boundary Layers at Gray-Zone Resolutions. *Monthly Weather Review, 143*(1), 250-271. https://doi.org/10.1175/MWR-D-14-00116.1

Sisterson, D., Peppler, R., Cress, T., Lamb, P., & Turner, D. (2016). The ARM southern great plains (SGP) site. *Meteorological Monographs, 57*, 6.1-6.14. https://doi.org/10.1175/AMSMONOGRAPHS-D-16-0004.1

Turner, A. J., Jacob, D. J., Wecht, K. J., Maasakkers, J. D., Lundgren, E., Andrews, A. E., et al. (2015). Estimating global and North American methane emissions with high spatial resolution using GOSAT satellite data. *Atmospheric Chemistry and Physics, 15*(12), 7049-7069. https://doi.org/10.5194/acp-15-7049-2015

References From the Supporting Information

Gifford, F. A. (1961). Use of routine meteorological observations for estimating atmospheric dispersion. *Nucl. Safety, 2*, 47-51.

Hu, X. M., Gourdji, S. M., Davis, K. J., Wang, Q., Zhang, Y., Xue, M., et al. (2021). Implementation of improved parameterization of terrestrial flux in WRF-VPRM improves the simulation of nighttime CO_2 peaks and a daytime CO_2 band ahead of a cold front. *Journal of Geophysical Research: Atmospheres, 126*(10), e2020JD034362. https://doi.org/10.1029/2020JD034362

Turner, D. B. (1967). *Workbook of atmospheric dispersion estimates* (Vol. 26): US Department of Health, Education, and Welfare, National Center for Air Pollution Control.